A New Algorithm for Sea Fog/Stratus Detection Using GMS-5 IR Data

Myoung-Hwan AHN *, Eun-Ha SOHN, and Byong-Jun HWANG

Remote Sensing Research Laboratory, Meteorological Research Institute,

Korean Meteorological Administration, Seoul 156-720, *Korea*

ABSTRACT

A new algorithm for the detection of fog/stratus over the ocean from the GMS-5 infrared (IR) channel data is presented. The new algorithm uses a clear-sky radiance composite map (CSCM) to compare the hourly observations of the IR radiance. The feasibility of the simple comparison is justified by the theoretical simulations of the fog effect on the measured radiance using a radiative transfer model. The simulation results show that the presence of fog can be detected provided the visibility is worse than 1 km and the background clear-sky radiances are accurate enough with known uncertainties. For the current study, an accurate CSCM is constructed using a modified spatial and temporal coherence method, which takes advantage of the high temporal resolution of the GMS-5 observations. The new algorithm is applied for the period of 10–12 May 1999, when heavy sea fog formed near the southwest coast of the Korean Peninsula. Comparisons of the fog/stratus index, defined as the difference between the measured and clear-sky brightness temperature, from the new algorithm to the results from other methods, such as the dual channel difference of NOAA/AVHRR and the earth albedo method, show a good agreement. The fog/stratus index also compares favorably with the ground observations of visibility and relative humidity. The general characteristics of the fog/stratus index and visibility are relatively well matched, although the relationship among the absolute values, the fog/stratus index, visibility, and relative humidity, varies with time. This variation is thought to be due to the variation of the atmospheric conditions and the characteristics of fog/stratus, which affect the derived fog/stratus index.

Key words: sea fog, GMS-5

1. Introduction

The poor visibility due to fog or low-lying stratus cloud (fog/stratus) results in many problems. Often, the poor visibility is responsible for severe losses to property and life due to traffic accidents and delays (Anthis and Cracknell, 1998). In Korea during 1998, there were 757 traffic accidents caused by low visibility, resulting in 99 deaths and 1412 injuries. Annually, about 500 airplane flights are delayed or cancelled due to poor visibility caused by fog. A study shows that about 39% (71 cases from a total of 184 accidents occurring from 1984 to 1988) of marine accidents such as shipwrecks and collisions are due to poor visibility (Kim, 1998), and the numbers have been increasing ever since. With the increase of marine activities and traffic around the Korean Peninsula, sea fog is an im-

portant subject for accurate forecasting.

The accuracy of fog forecasting, in areas such as the formation and dissipation time and visibility, is limited due to many causes (Croft et al., 1997), including the limited ability of accurate observations. The detection of fog over land is routinely made at weather stations, although an accurate observation is usually limited to the daytime and to the areas nearby the stations. Even worse, only one of the weather stations in Korea began to measure the microphysical parameters of fog such as the size distribution, vertical distribution, and optical properties of fog from July 2002. The state of fog observations over open ocean is much worse than over land. Sea fog detection relies mainly on reports from cruise ships and lighthouses and the reports are very limited in terms of frequency and accuracy.

For detection of fog extending to a large area, at

nighttime, and over ocean, satellites are the only possible tool, although they have their own limitations. During the daytime, fog can be detected from satellites with relative ease because of the clear contrast in the measured albedo and brightness temperatures of the foggy and ambient clear areas. Areas of fog are characteristically bright in the visible image (VIS) and relatively cool in the infrared image (IR), while the clear region is characterized as dark in the visible and warm in the infrared image. However, during the nighttime it is difficult to detect fog because of the absence of the visible channel and the relatively small thermal contrast between foggy and clear areas (Ernst, 1975). Thus, during the nighttime, a different approach, using the brightness temperature difference between two channels that have different optical responses to the presence of fog, was developed. For example, the dual channel difference (DCD) method, taking the difference between NOAA/AVHRR 3.7-μm and 11-μm channel brightness temperatures ($T_{b3.7} - T_{b11}$), has been widely used for nighttime fog detection (Eyre et al., 1984; Saunders and Kriebel, 1988). The DCD method has also been adopted for the geostationary satellites, such as the GOES series, that have a 3.9-μm channel (Ellrod, 1995; Lee et al., 1997) to detect low-lying cloud decks. Use of the geostationary satellites made it possible to monitor fog 24 hours a day. Ellrod (1995) shows that the DCD method could delineate stratiform clouds over various conditions and suggested a possible link between the magnitude of DCD and the thickness of fog.

In Korea, the DCD method has been successfully applied to the NOAA direct readout data, although the method is applicable only once a day due to the limitations caused by the combination of satellite pass time and contamination of the 3.7-μm channel by the reflected sunlight (METRI, 1999). However, for continuous and effective monitoring of fog/stratus cloud, continuous detection, which is highly necessary, could be provided by a geostationary satellite. Over the Korean Peninsula, hourly observations made by the GMS-5 could be used. However, as the GMS-5 is not equipped with the 3.7-μm channel, a method is required to delineate fog/stratus with other infrared channels such as the 6.9-μm water vapor channel, and the 11-and 12-μm split-window channels.

The new method compares the measured radiance with a predetermined, accurate clear-sky radiance composite map (hereafter called CSCM) of GMS-5 11-μm brightness temperature (T_{b11}). The construction of CSCM takes advantage of the high temporal resolution of GMS-5, 28 times a day (24 hourly observations and four half-hourly observations for cloud drift wind calculation). An effective utilization of high frequency GMS-5 observations is made through the spatial-temporal coherence tests of radiance for a small area. An accurate CSCM is obtained only over the sea, where the variation of clear sky brightness temperature is relatively small. A detailed discussion of the CSCM construction and examples are shown in section 2. Section 3 shows some results from the application of the new method. The paper is concluded in section 4.

2. The new method

The new method is based on the fact that when fog/stratus is present in the lower atmosphere, T_b in the window channels is often lower than that of the clear sky, especially over oceans. For the clear sky, the surface skin temperature and some reductions caused by the weak water vapor absorption mainly determine the observed T_b in the window channel. However, when fog/stratus is present in the field of view (FOV), the cloud traps the surface-emitted upward radiation where the amount of the trapping is mainly determined by the optical thickness of the cloud. Thus the major part of the radiation reaching the satellite is from the fog/stratus, which often has a lower temperature than that of the surface, resulting in less radiation reaching the satellite. Thus, if the presence of fog/stratus produces a significant temperature contrast compared to the clear ambient value, a simple comparison between the measured T_b and clear-sky T_b could be used to detect the presence of fog/stratus.

To estimate the effect on the measured T_b by the presence of fog/stratus, we simulate the upwelling radiance at the top of the atmosphere with a radiative transfer model, MODerate-resolution TRANsmittance code (MODTRAN, Anderson et al., 1995) and known boundary and atmospheric conditions. T_b is calculated with the band-averaged radiance, obtained by the spectral radiances and the GMS-5 channel response function (MSC, 1997). As the microphysical parameters of fog near the Korean Peninsula, such as the size distribution, are not known very well, we use the two fog models imbedded in the MODTRAN3.7. For the vertical profile and visibility simulation, we use the Army Vertical Structure Algorithm (Anderson et al., 1995). Also, to see the air temperature and humidity effects on the T_b, we simulate several different sets of atmospheric conditions, each having its own characteristic vertical profiles of temperature and humidity, with ocean boundary.

Figure 1 shows the effect of fog on T_{b11} for the three different standard atmospheres, mid-latitude winter, mid-latitude summer, and 1976 U. S. Standard. Each
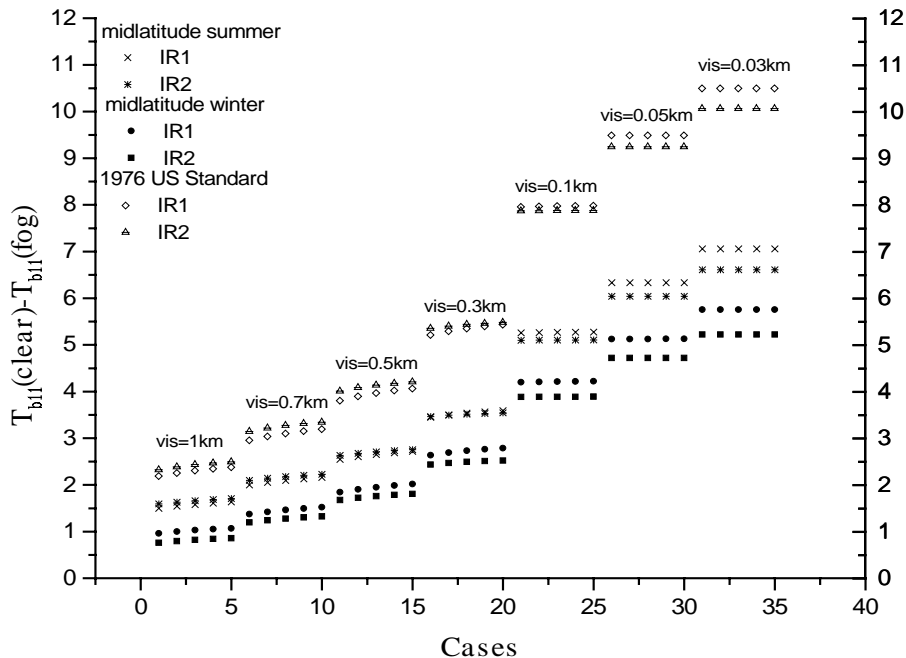
Fig. 1. Fog effect on the measured $T_{\rm b}$ for three different standard atmospheres, mid-latitude winter, mid-latitude summer, and 1976 U.S. Standard. Different cases are for different cloud top altitudes (50, 100, 200, 300, and 400 meters) with the same visibility. IR1 and IR2 denote the brightness temperatures at 11 and 12 μm of GMS-5, respectively.

point represents the $T_{\rm b11}$ difference between the clear and foggy conditions for a combination of different visibilities and thickness of fog. The presence of fog reduces $T_{\rm b11}$ for all atmospheric conditions. The magnitude of the reduction depends on the opacity of fog, determined by visibility rather than the geometrical thickness of the fog, implying that the effect on the $T_{\rm b11}$ is expected to be mostly sensitive to the visibility of fog. This implies the size of fog particles is much smaller than that of mid to high altitude water cloud. In the same figure, $T_{\rm b12}$ is also shown to emphasize that the channel difference is not significant when fog is present, being mostly less than 0.5°C.

In the case of the mid-latitude summer atmospheric profile, when the visibility is only 50 m, the measured $T_{\rm b11}$ is colder than the clear-sky $T_{\rm b11}$ by about 6°C, which implies that the presence of fog could easily be detected by a simple comparison to the clear sky $T_{\rm b11}$. However, when the visibility is better than 1 km, the temperature difference is only about 1.5°C and the presence of fog would not be easily discernable from a clear ambient surface. The fog effect depends also on the temperature profile, which is larger in summer than in winter, and on geographical characteristics including the temperature of the ocean surface. Therefore, to determine appropriate upper threshold values

for fog detection, we may need the real-time observation of the vertical atmospheric profile. However, for the decision of the presence of fog/stratus, a simple comparison of the brightness temperature seems to give reasonable results.

The seemingly large $T_{\rm b}$ decrease due to the presence of fog is due to two factors: less emission of upwelling radiance by a cooler fog top, and decrease of path thermal emission by the low-lying water vapor. Figure 2 shows each component of the upwelling clear sky radiance, surface emission, path thermal, and thermal scattering, at the top of the atmosphere as a function of wavenumber for the midlatitude summer profiles of temperature and humidity. Although most of the total upwelling radiance comes from the surface emission (about 90 %), a non-negligible portion of the radiance also comes from the path thermal emission (about 9 %), which is mainly from the water vapor, and a small portion of the radiance is from the thermal scattering (about 1 %). Thus even when the sky is clear, due to the absorption and reemission of upwelling radiation by water vapor, the measured $T_{\rm b}$ is 291.7 K, whereas the boundary temperature is 294.3 K.

When fog is present in the lower atmosphere, fog absorbs almost all surface and water vapor emissions
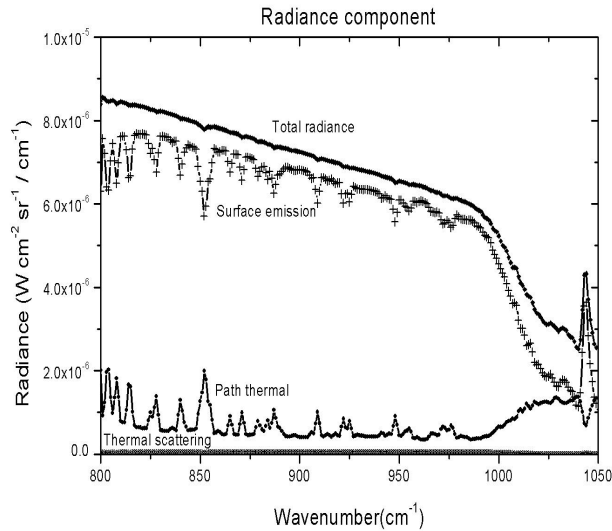
Fig. 2. Contribution to the difference by the presence of fog in the upwelling radiance at the top of the atmosphere by the surface emission, path thermal, and thermal scattering as a function of wavenumber. The visibility and top altitude of fog are assumed to be 1 km and 300 m, respectively.
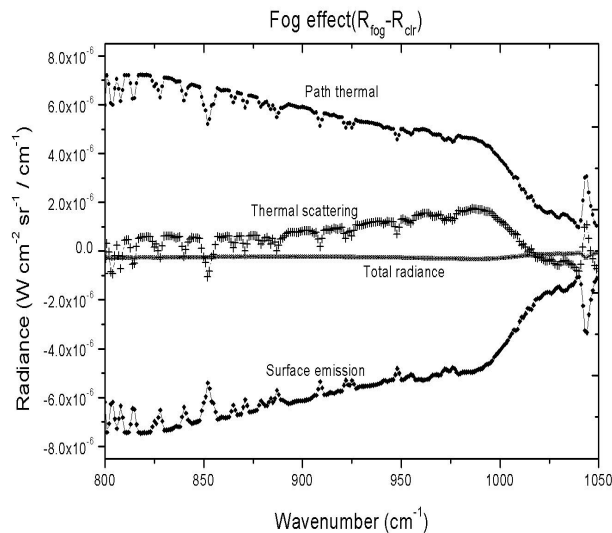

Fig. 3. The fog effects on each component of the upwelling radiance measured at the top of the atmosphere for the midlatitude summer temperature and moisture profiles with a visibility of 200 m.

below the fog top, resulting in much less total upwelling radiance than that of clear sky if the temperature at the top of the fog is cooler than that of surface. Figure 3 shows the fog effects on each component of upwelling radiance measured at the top of the atmosphere with a visibility of 200 m. The total reduction of radiance is about 0.4×10^{-6} W cm^{-2} sr^{-1}/ cm^{-1} (about a 5% reduction), which corresponds to about

a 4.0-K decrease in $T_{\rm b}$. The decrease of total radiance is mainly due to the decreased contribution by the surface emission. The reduction is compensated for by the increased contribution of the path thermal and thermal scattering by fog. In the radiative transfer calculation, fog is treated as an addition of absorbing mass instead of as a boundary such as the sea surface. Thus, the increased contribution by path thermal is mainly due to the emissions by fog. As the moisture is mainly found in the lower atmosphere, the contribution of water vapor emission to the total radiance is also removed because of the strong absorption by the fog. Thus, the decreased $T_{\rm b}$ is caused by the reduced contribution of surface emission and water vapor emission. However, it should be noted here that the effect would be smaller if a significant amount of water vapor resides above the fog layer.

From the simulation results, we conclude that the detection of fog/stratus by using the simple comparison is feasible when the visibility of fog is very low with the top temperature cooler than the surface and when we have the clear-sky brightness temperatures with the uncertainties lower than the actual signal of the fog/stratus. We also conclude that the dual-channel difference between the split-window channels does not give an appreciable improvement in the detection of fog/stratus because the overall spectral responses of fog to the split-window channels are almost the same. However, it should be mentioned here that the split-window channel difference is much smaller for fog/stratus than for a large amount of water vapor loading. The construction of an accurate CSCM with a known uncertainty is explained in the next section.

2.1　Clear sky radiance composite map

The most important step in the new method is the construction of an accurate CSCM. To take advantage of the high temporal resolution of the GMS-5 observations, we adopt a spatial-temporal coherence method, which tests both the spatial (Coakley and Bretherton, 1982) and temporal (Coakley and Baldwin, 1984) coherence of the measured $T_{\rm b11}$. Figure 4 shows the flow chart of the overall process of the new algorithm. We first select potential clear-sky $T_{\rm b11}$ by testing spatial and temporal uniformity. Then we refine the potential clear-sky $T_{\rm b11}$ through a simple inspection of the histogram of the potential clear-sky $T_{\rm b11}$. The current method accumulates mean and standard deviation in terms of time instead of space, which is adopted by most of the spatial coherence methods (Coakley and Bretherton, 1982, and others). Finally, the presence of fog is detected by a comparison between CSCM and measured $T_{\rm b11}$. The broken clouds and edge of the
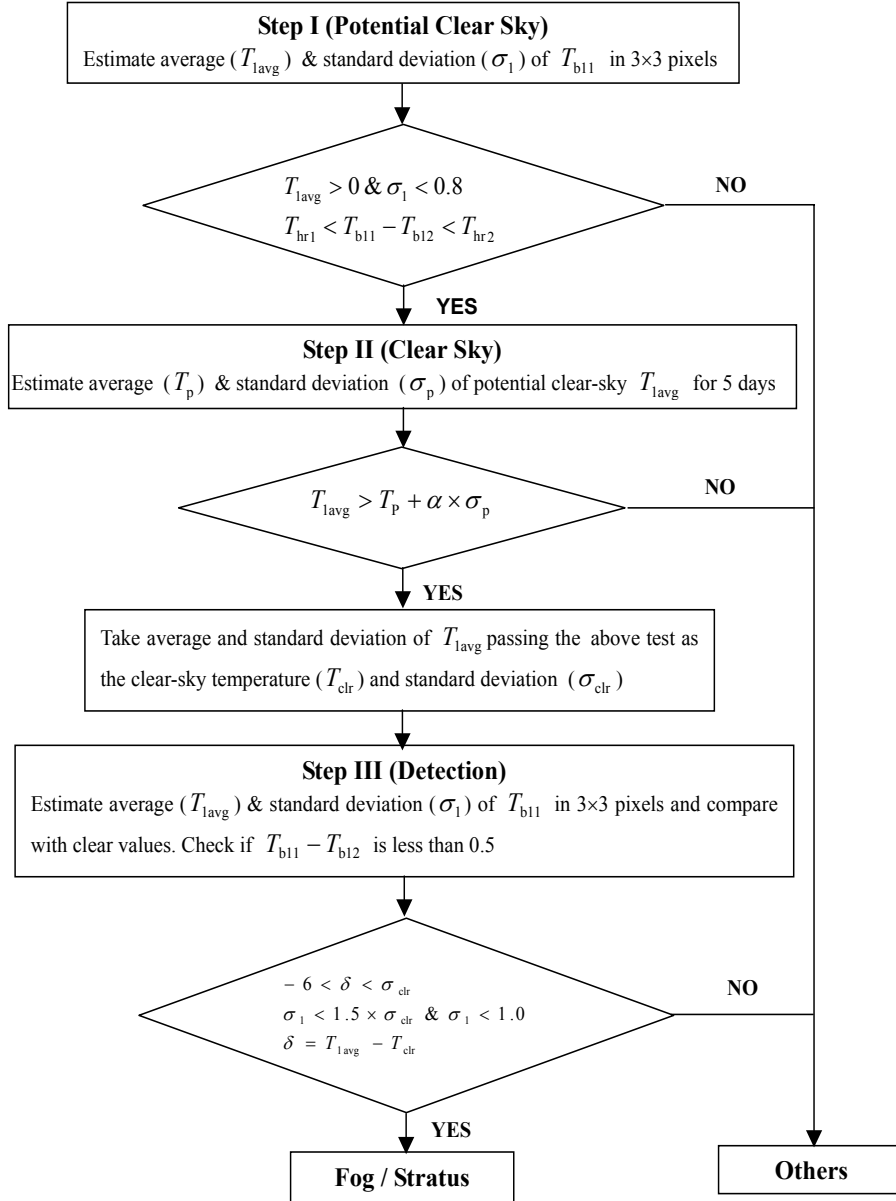

Step I (Potential Clear Sky)
Estimate average (T_{lavg}) & standard deviation (σ_1) of T_{b11} in 3×3 pixels

$T_{\mathrm{lavg}} > 0 \, \& \, \sigma_1 < 0.8$
$T_{\mathrm{hr1}} < T_{\mathrm{b11}} - T_{\mathrm{b12}} < T_{\mathrm{hr2}}$

NO

YES

Step II (Clear Sky)
Estimate average (T_{p}) & standard deviation (σ_{p}) of potential clear-sky T_{lavg} for 5 days

$T_{\mathrm{lavg}} > T_{\mathrm{p}} + \alpha \times \sigma_{\mathrm{p}}$

NO

YES

Take average and standard deviation of T_{lavg} passing the above test as the clear-sky temperature (T_{clr}) and standard deviation (σ_{clr})

Step III (Detection)
Estimate average (T_{lavg}) & standard deviation (σ_1) of T_{b11} in 3×3 pixels and compare with clear values. Check if $T_{\mathrm{b11}} - T_{\mathrm{b12}}$ is less than 0.5

$-6 < \delta < \sigma_{\mathrm{clr}}$
$\sigma_1 < 1.5 \times \sigma_{\mathrm{clr}} \, \& \, \sigma_1 < 1.0$
$\delta = T_{\mathrm{lavg}} - T_{\mathrm{clr}}$

NO

YES

Fog / Stratus

Others

Fig. 4. Flow chart of the overall process of the new algorithm. Step I and Step II are for the construction of the clear-sky composite map and Step III is for the detection of fog/stratus. The T_{hr1} and T_{hr2} are the threshold for cirrus detection (Yasuda and Shirakawa, 1999), α is 0.5 if $T_{\max} - T_{\mathrm{lavg}}$ is larger than 2, and is 0 otherwise.

cloud deck are removed by checking the standard deviation of a small area of 3×3 pixels. The split-window test is used for the detection of high water vapor regions, possible heavy dust loading, and possible cirrus clouds (Inoue, 1985; Yasuda and Shirakawa, 1999).

To obtain the potential clear-sky T_{b11}, we calculate the average and standard deviation of T_{b11} within a 3×3 pixel-box at a given time, and accumulate these values for a 5-day time period. Figure 5 shows the scatter diagram constructed by the accumulation of points

for the average and standard deviations of T_{b11} for 5 days, for a total of 120 points. The spatially uniform features, such as clear sky over a uniform background or dense cloud deck, will have a smaller standard deviation within the small box (Coakley and Bretherton, 1982). Thus, we select points having a standard deviation less than a threshold value. Here, we note that the temporal variation of the measured T_{b11} over the land is so large, due to the diurnal variation of surface temperature, that we apply the new method only over
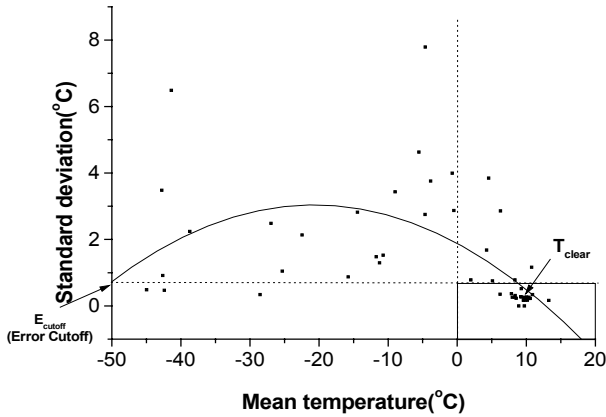
Fig. 5. Accumulated T_{mean} and standard deviation within a small area of 3×3 pixels, for 5 days at one pixel point.
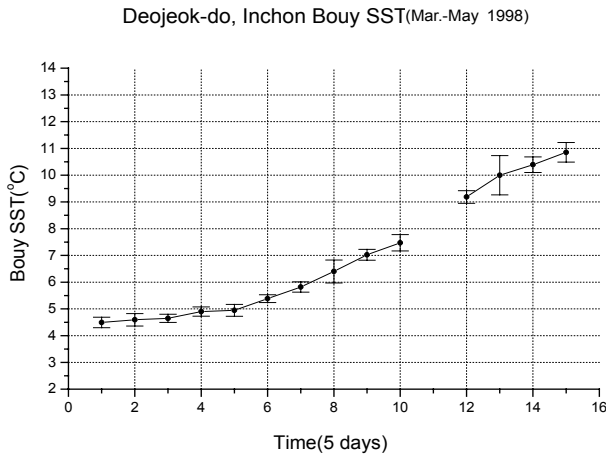

Fig. 6. Temporal variation of the sea surface temperature off the west coast of Korea obtained by a buoy at Deokjeok-do, near Inchon, in the Yellow Sea. Error bars represent the standard deviation.
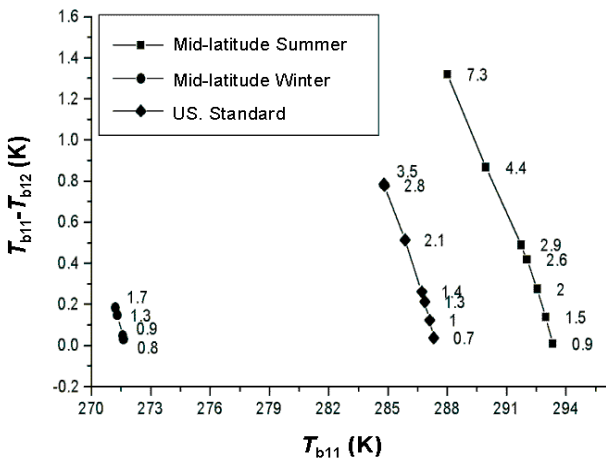

Fig. 7. The calculated relationship among water vapor amount (g cm^{-2}, numbers beside the line), T_{b11}, and $T_{b11} - T_{b12}$ for the three standard atmospheres: midlatitude winter and summer, and U.S standard atmosphere.

the ocean by assuming that the temporal variation of the sea surface temperature (SST) is fairly small. Figure 6 shows the temporal variation of the SST on the west coast of the Korean Peninsula observed by a moored buoy. The estimated SST variation (one standard deviation) is about 0.5°C/5 days, which is fairly small compared to the variation caused by the atmospheric perturbations such as the cloud and water vapor contents.

We determine the threshold value by considering factors that contribute to the observed variation in the clear region. When the pixels are cloud free, the variation of T_{b11} within the 3×3 pixels is mainly due to the instrument noise, variation of water vapor content and sea surface temperature, and emissivity of the ocean surface. We consider that the spatial variability of T_{b11} due to the variation of the sea surface emissivity is small enough to be neglected (Masuda et al., 1988), although some regions, such as the coastal regions where there is a large influx of fresh water, have a highly variable emissivity. The instrument noise of GMS-5 is reported to be about 0.35 K (MSC, 1997). The spatial variability of SST is relatively small except for the regions where an active mixing and upwelling occur. The active mixing occurs in areas such as those over the frontal regions (Park, 1996), where the temperature gradient is estimated to be about 0.1–0.15 °C km^{-1} (Roden, 1975).

The most unknown variability in the T_{b11} within the small area is due to the variability of the water vapor contents, which is not easily estimated. We use the channel difference of T_{b11} and T_{b12} for a surrogate of the water vapor contents. We vary the threshold standard deviation (E_{cutoff}) in step I and estimate the mean and standard deviation of the channel difference for 5 days. As shown in Table 1, the standard deviation is about 0.15°C, and is remarkably constant regardless of the threshold values. To estimate the variability of T_{b11} corresponding to the variability of the channel difference, we use the radiative transfer model. Figure 7 shows the estimated relationships among the moisture, $T_{b11} - T_{b12}$, and T_{b11} for three different atmospheric profile. The numbers on each line denote the column water vapor amount embedded in each standard temperature profile. In the simulation, we vary the water vapor profile proportionally to give the total column amount without varying the temperature profile. The channel difference ($T_{b11} - T_{b12}$) increases with the increasing column water vapor, while the individual channel temperature decreases with the increasing column water vapor for all three atmospheres. The slope shows the relationship between the channel
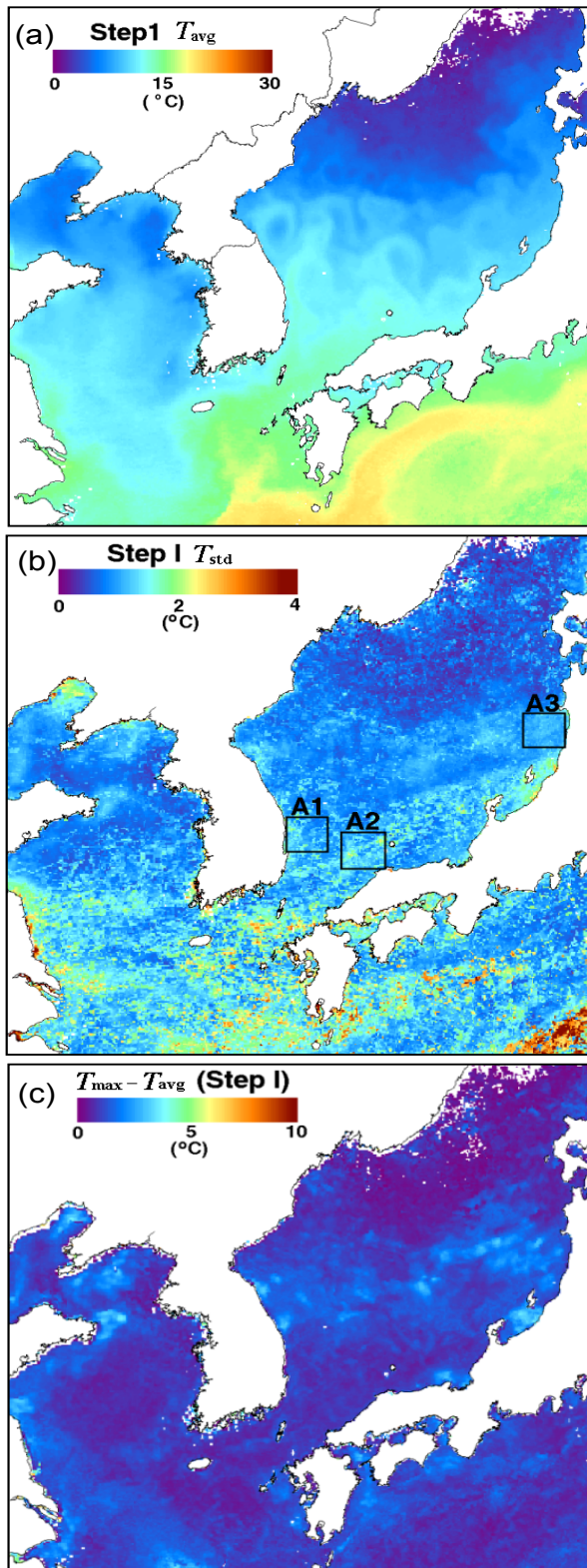
Fig. 8. Potential clear-sky T_{b11}, its standard deviation, and difference between maximum T_{b11} and the potential clear-sky T_{b11} for a 5-day period from 6–10 May 1999.

difference and moisture effect on the measured T_{b11}; the values are –0.28, –0.35, and –0.38 for the Midlatitude Summer, U.S Standard, and Midlatitude Winter Atmospheres, respectively. The variation is thought to be due to the difference in temperature profile and absolute amounts of water vapor contents in each standard atmosphere. Using the relationship, we estimate the variability of T_{b11} due to the variability of the water vapor to be about 0.6°C at maximum.

As the variability of T_{b11} by the three factors can be considered to be independent, the expected variability by the clear sky condition is assumed to be the root mean square value of all three components, 0.35, 0.3, and 0.6°C, which is about 0.8°C. We also assume the clear-sky T_{b11} is larger than 0°C on the basis of the actual SST over the regions of interest being above the freezing temperature. Thus, for the first step in the construction of the CSCM, we select only data having a positive mean T_{b11} and a standard deviation of less than 0.8°C as a clear sky pixel, with the points within the box in Fig. 5 being potential clear-sky values. The selected data is further screened by using the measured albedo for daytime data. If the measured albedo is larger than 0.05, we assume that the data is contaminated by clouds.

Figure 8 shows the distribution of the potential clear sky brightness temperature and its standard deviation for the period of 5–10 May 1999. The mean T_{b11} field, Fig. 8a, shows well-developed ocean eddies along the polar fronts across the east coast of the Korean Peninsula to the west coast of Japan. The northern part of the East Sea (Japan Sea) near Okhotsk has a T_{b11} value of around 0°C, while it is about 20°C at the center of the Kuroshio Current. For a simple comparison, the weekly averaged SST made from the direct broadcast NOAA/AVHRR is shown in Fig. 9. Although the absolute values of the two fields do not agree completely, the overall pattern is almost the same. The SST at the center of the Kuroshio Current is about 25°C while the clear-sky T_{b11} is only about 20°C, which is due to the atmospheric water vapor effects.

The general feature of the standard deviation, Fig. 8b, is similar with what is expected, namely less than 1°C over most regions and with several areas having a much larger variation. The areas with a large standard deviation, marked as AREA1, AREA2, and AREA3, have a maximum of about 4°C, near the middle of the east coast of the Korean Peninsula, north of Okayama, and southwest of Hokkaido. AREA1 and AREA2 correspond to the areas where cold ocean flows intrude to the warm ocean body along the coastline, while AREA3 corresponds to the area affected by the persistent sea fog. These areas are also well correlated
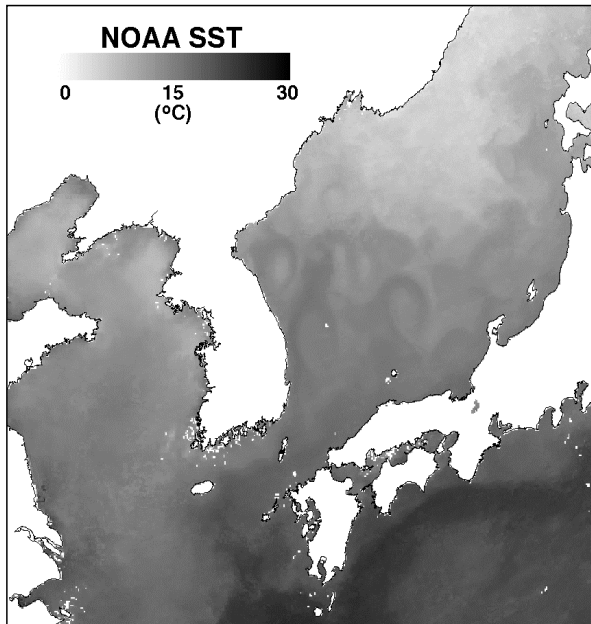
Fig. 9. Weekly averaged NOAA SST for the period 6–13 May 1999.

with the regions having a large difference between the maximum $T_{b11}(T_{max})$ and average $T_{b11}(T_{avg})$ of the 5-day period, shown in Fig. 8c.

The next step is refining the mean T_{b11} obtained from the first step. As shown in Fig. 8c, the distributions of the selected potential clear-sky T_{b11} are quite different depending on the degree of contamination by factors such as the low-lying uniform clouds, the small fraction of broken cloud, and the temporal variation of sea surface temperature. The contamination by low-lying uniform clouds cannot be easily removed by the coherence approach, which requires a further refinement of the potential clear-sky T_{b11}.

The unfiltered broken clouds or uniform warm clouds are removed by using the difference between the maximum $T_{b11}(T_{max})$ during the given time period and mean $T_{b11}(T_{avg})$. If the $T_{max} - T_{avg}$ is larger than a threshold value, $2°C$ for the current study, we select temperatures larger than the T_{avg} as the clear-sky pixel and average them for the final clear-sky composite map. If the $T_{max} - T_{avg}$ is less than the threshold value, we choose temperatures larger than $T_{avg} - 0.5 \times \sigma_1$ as the clear-sky T_{b11}, with σ_1 being the standard deviation of the potential clear-sky T_{b11}. In order to obtain reliable statistics, we choose clear-sky T_{b11} only when the number of data points is more than 5.

Figure 10 shows the constructed CSCM and standard deviation of the clear-sky radiance value at each pixel for 10 May 1999 that represent the ocean eddies and polar front in the East Sea remarkably well. The Kuroshio Current and mesoscale eddies south of Japan

and in the middle of the East Sea are clearly seen. The large standard deviation, Fig. 10b, shown in this area may be caused by the movement of the mesoscale ocean eddies. Persistent cloud covering the northeast part of the East Sea and southwest part of Jeju Island also increases the standard deviation in these regions. Table 2 shows the area-averaged T_{b11} and standard deviation of the clear-sky T_{b11} from Step I and Step II for the three areas shown in Fig. 8. The standard deviation is reduced by as much as $2°C$ and the clear-sky T_{b11} increases about by $1°C$.

2.2 Detection of fog/stratus

The first step for the actual detection of fog/stratus is the construction of the 3×3 pixel average and standard deviation and comparison with the CSCM. Figure 11a shows the T_{b11} image at 1930 UTC 10 May 1999. It shows clouds associated with the frontal system located over the ocean south of Japan and few high clouds over the Yellow Sea. Figure 11b shows the difference between the measured T_{b11} and the clear-sky T_{b11}. Possible cloudy areas, which were not clearly shown in Fig. 11a, are revealed in the difference image, i.e. the increase of difference implies the decrease of the measured T_{b11} due to the presence of clouds. There are regions having temperature differences of more than $6°C$ where the IR imagery clearly shows thick clouds. Thus we choose another threshold value to delineate middle and high clouds from the temperature difference field. As shown in Fig. 1, the fog effect on the T_{b11} is about $6°C$ at maximum when the visibility is only 50 m. Thus, we choose $6°C$ as the largest temperature difference for the mid-latitude summer atmospheric condition.

Even after removing the mid- to high-level clouds by using the threshold value, there are still some regions classified as fog/stratus regions where the close inspection of IR imagery says the opposite. These regions are associated with the cloud edge and broken clouds. Thus we use the measured standard deviation of T_{b11} within the 3×3 pixels to remove broken cloud and cloud edges. If the standard deviation is larger than the variation of the clear-sky radiance and expected variance over the uniform fog/stratus top, we consider that the broken clouds contaminate those pixels. For the uniformity test we use the threshold value of $0.8°C$ used for the CSCM generation.

Finally, we apply the channel difference for the cirrus cloud detection (Inoue, 1985) with the new threshold values (Yasuda and Shirakawa, 1999). We also found that the channel difference could be used to delineate the high water vapor loaded area from the fog/stratus region. When a large amount of water vapor is present in a FOV, the measured T_b can be reduc-

Table 1. The variation of standard deviation of brightness temperature difference between 11 and 12 μm of GMS-5 as a function of the threshold standard deviation (see text)

Date	10 May 1999		27 May 1999	
E_{cutoff}	$\sigma\,(\Delta T_{12})$	mean (ΔT_{12})	$\sigma\,(\Delta T_{12})$	mean (ΔT_{12})
0.6	0.145	1.04	0.149	0.83
0.7	0.145	1.05	0.149	0.84
0.8	0.145	1.06	0.150	0.86
0.9	0.145	1.00	0.150	0.87
1.0	0.145	1.07	0.150	0.88
1.2	0.145	1.08	0.150	0.90

Table 2. The area averaged $T_{\mathrm{b}11}$ and the standard deviation of the clear-sky $T_{\mathrm{b}11}$ from the Step I and Step II for the three areas shown in Figure 8

	Step1 (Potential Clear Sky)		Step 2(Clear-Sky Composite Map)	
	Average	Standard	Average	Standard
AREA 1	10.5	2.7	11.7	0.6
AREA 2	11.5	2.4	12.5	0.4
AREA 3	4.9	2.5	6.7	0.4
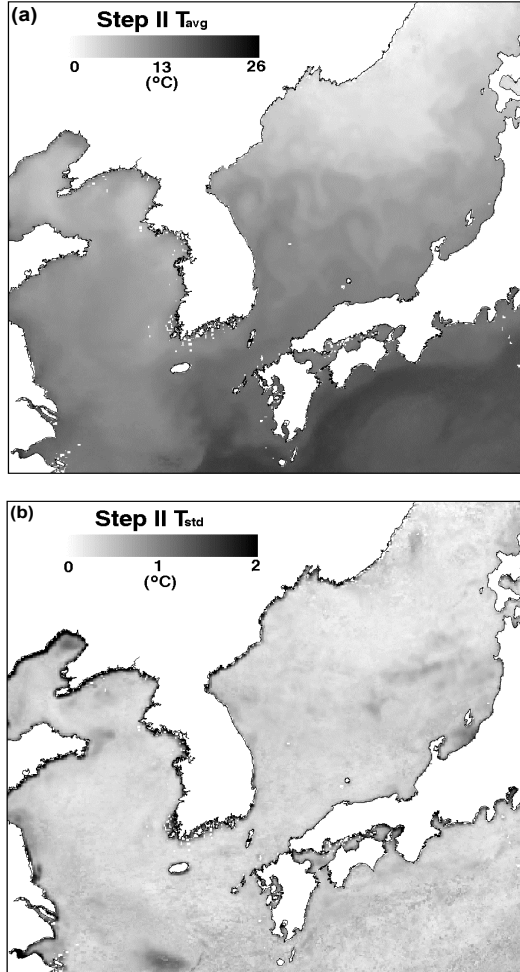
Fig. 10. Clear-sky radiance composite map and its standard deviation distribution on 10 May 1999.

ed significantly which results in a false detection of fog/stratus. As shown in Fig. 1, in most of case, the $T_{\mathrm{b}11} - T_{\mathrm{b}12}$ is smaller than 0.5 K for when the fog/stratus is present, while it can be much larger when a large amount of water vapor is present. Thus for a final test, we check the $T_{\mathrm{b}11} - T_{\mathrm{b}12}$ value which should be less than 0.35 K, which is the GMS-5 noise equivalent temperature, to be determined as the fog/stratus area.

Figure 11c shows the final imagery of the fog index defined as the T_{b} difference between the instantaneous measurement and the CSCM on 10 May 1999. Large areas of possible sea fog are detected along the west coast of Korea, and in the South Sea. For the case of foggy areas on the west coast of Korea, the maximum fog index is about 3°C and the index increases toward the center, which might suggest a decrease of visibility. In the next section, we show the application results with some comparisons between the results from the current study and other methods, such as the DCD method and earth albedo method (METRI, 1999).

3. Validations

The validation of the new algorithm could be done through the direct comparison to the actual observations of visibility. However, as the direct observation of visibility over the ocean is not readily available, we use the results from other detection methods such as the NOAA/DCD method, and the limited number of visibility measurements from the weather stations near the ocean. We apply the new algorithm for the period of 9–12 May 1999 when a dense sea fog formed near
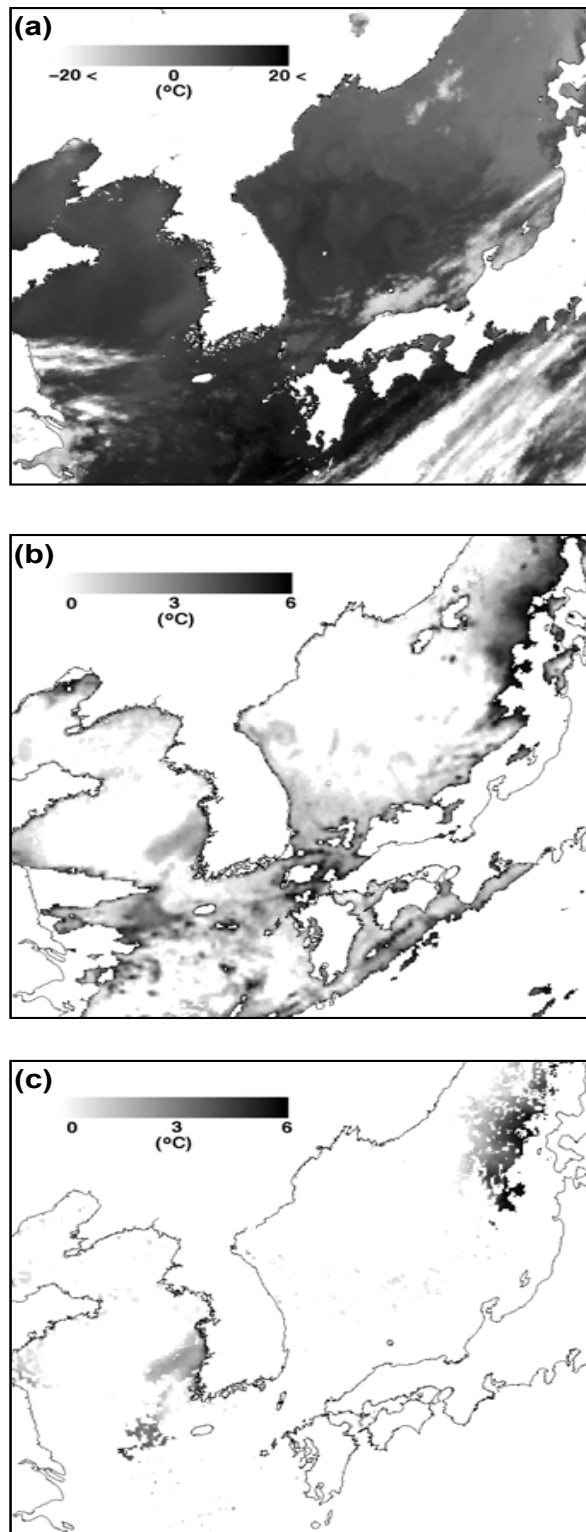
Fig. 11. The IR imagery and temperature difference from the clear-sky composite map (a), a possible fog/stratus area after limiting the temperature difference to be less than 6°C (b), and detected fog/stratus imagery after applying the spatial uniformity and cirrus test (c).

the Korean Peninsula, especially along the west coast of the peninsula.

Figure 12 shows the detected fog/stratus area from the current study and the NOAA/DCD method for 4 days, from 9–12 May 1999. We shade the fog index, $T_{b11} - T_{clear}$, when it is larger than the uncertainty of the clear-sky T_b, and smaller than –6°C to indicate a possible fog area. The shaded area in the NOAA/DCD imagery is where the DCD is negative, specifically –3.5°C to –9°C, which are empirically derived threshold values for the fog detection. The threshold value is colder than that of the generally used threshold value, –2°C (Lee et al., 1997; Eyre et al., 1984), and closer to the boundary between stratus/fog and cloud-free desert land (Lee et al., 1997). Thus, it is highly possible that the current DCD method would detect a strong and dense fog over the ocean but miss a weak fog. During the four days, the fog area detected from the GMS-5 observation matches well with the results from the NOAA/DCD method in terms of shape and location. As the DCD method can be used over land, a large area in the southern part of the Korean Peninsula is also detected as a foggy area where the ground observations indeed reported low visibility (not shown). The magnitudes of both the DCD and fog index increase toward the center of the fog/stratus and decrease toward the boundary. Although the index could be used for the derivation of visibility (Lee et al., 1997), we did not attempt to derive the visibility simply because of the uncertainties in the index, as explained in section 1.

During the daytime, the results from the current method can be compared directly with the visible imagery. Figure 13 shows the detected fog/stratus area from the current method along with the visible imagery at 0330 UTC 10 May 1999. Generally, the two results match remarkably well. The fog/stratus along the west coast of Korea shown according to the earth albedo method is well reproduced by the current method and the fog/stratus in the sea southwest of Jeju Island is also detected from both methods.

The ground-measured visibility and relative humidity at the Mokpo weather station, which is located on the southwest coast of the Peninsula, with the collocated T_b difference for the period of 10–12 May 1999 are shown in Fig. 14. The correlation among the low visibility, high relative humidity, and fog index is clearly seen. When the visibility is lower than 1 km, the relative humidity is higher than 90% and the fog index is about 1.5; that is the same value as the simulation result. During the nighttime of 10 May 1999, the visibility is worse than 0.5 km and the fog index is about 2. Although the specific time of the beginning
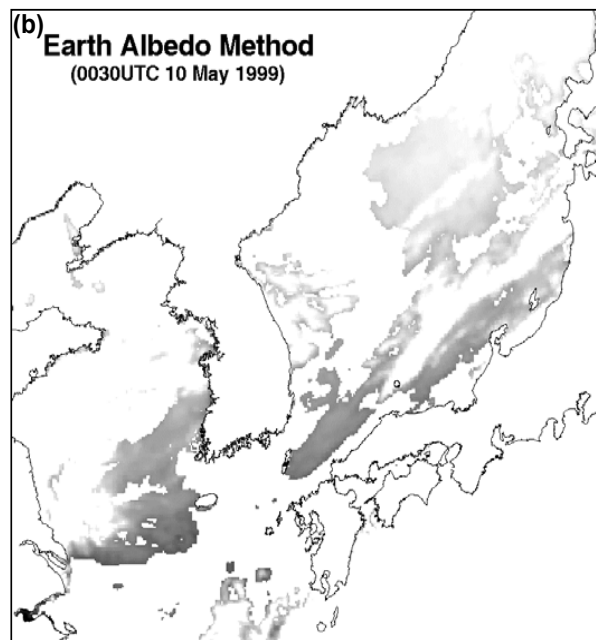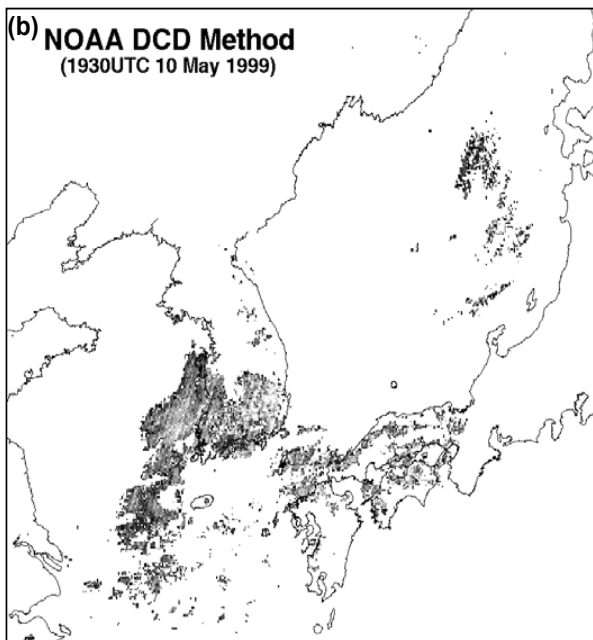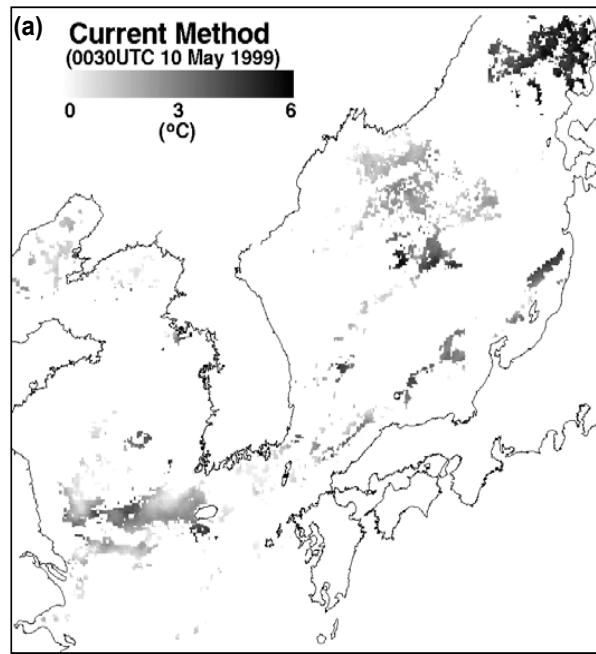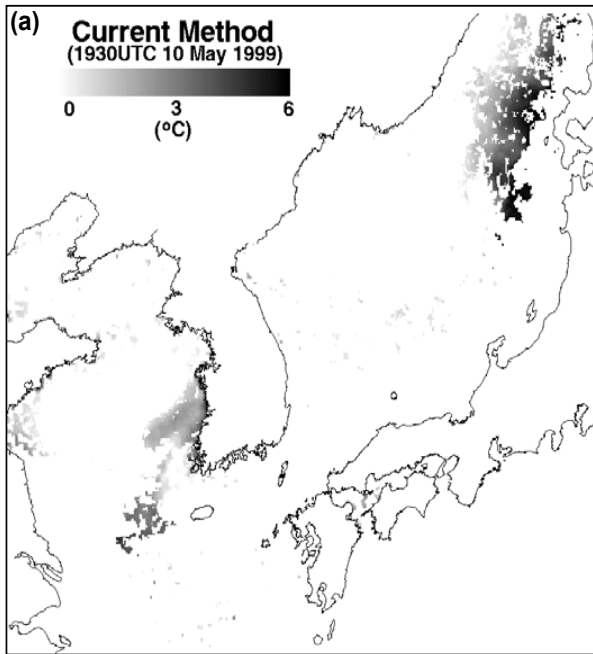
Fig. 12. Fog/stratus area detected by (a) the current method (GMS-5 IR data) and (b) the brightness temperature difference between 3.9 and 11 μm of NOAA/AVHRR. The possible fog/stratus area is shaded.

Fig. 13. Fog/stratus area detected by (a) the current method (GMS-5 IR data) and (b) the earth albedo method. The possible fog/stratus area is shaded.

and ending of low visibility are not matched exactly with the high fog index, the general trends of relative humidity and fog index are well matched.

Figure 15 shows the series of the fog/stratus area detected by the new method during 10–12 May 1999 every 3 hours. The formation and dissipation of fog/

stratus in the Yellow Sea are clearly shown. On 10 May 1999, there is no significant area of fog/stratus on the west coast of the Korean Peninsula until 0630 UTC 10 May. The fog begins to form in the evening of 10 May, continually developing during the nighttime, with a very clear shaping and extension of the fog area
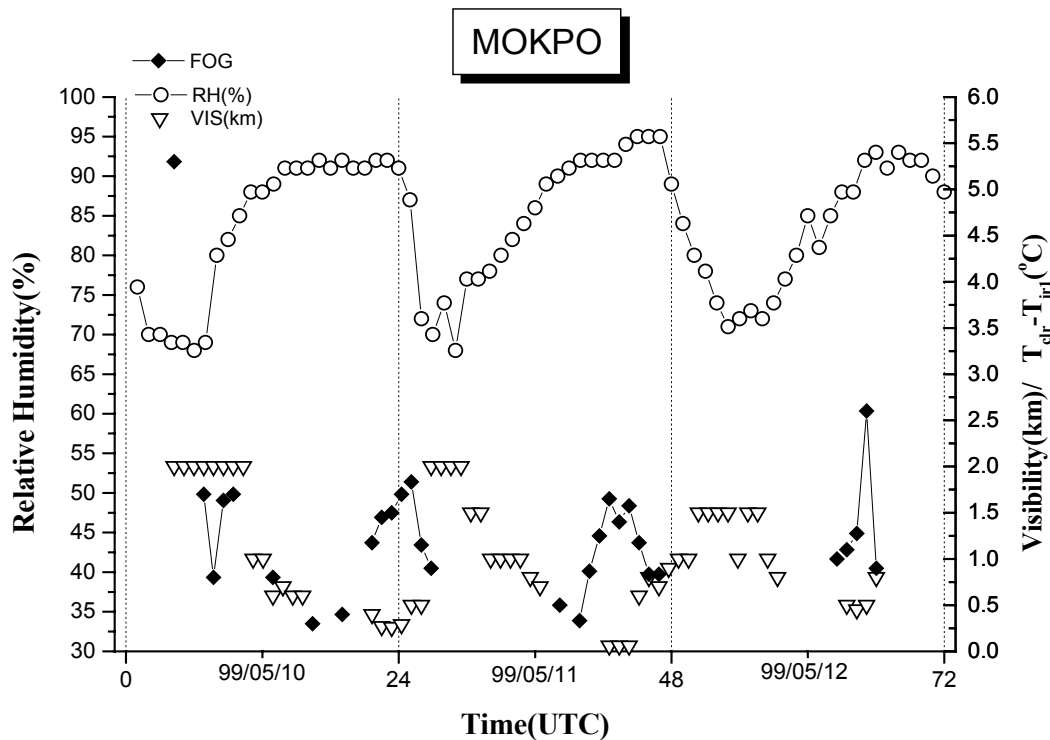
Fig. 14. A time series of ground measured visibility, relative humidity, and collocated T_{b11} difference at Mokpo airport, located in the southwest part of the Korean Peninsula, from 10–12 May 1999.

until 0330 UTC. During the daytime of 11 May, the fog begins to dissipate and becomes clear after 0630 UTC until 0930 UTC 11 May. At 1830 UTC 11 May, a small area of fog forms and lasts until 0030 UTC of the next day. During the daytime of 12 May, no significant fog is formed. The formation of fog/stratus during the nighttime in this specific time period is thought to be related to the advection of cold air over the warm ocean (not shown), while the dissipation of fog/stratus during the daytime is related to the radiative forcing.

4. Discussions and conclusion

While the nighttime sea fog/stratus causes a severe condition in marine activities, forecasting its formation and dissipation is very difficult, partly due to the lack of observation. Only the satellite observations can be used for the continuous monitoring of fog/stratus in the areas where direct observation is not possible. For the purpose of continuous monitoring, a geostationary satellite is more effective than the polar orbiters. The high sensitivity of the 3.7-μm channel in NOAA/AVHRR and GOES to the presence of fog/stratus has been extensively used for nighttime fog/stratus detection. However, the current GMS-5

satellite is not equipped with the fog sensitive channel and a new method using T_{b11} has been developed here.

The new method, using a simple comparison between the measured and clear-sky brightness temperature, is highly dependent on the accuracy of CSCM. Construction of an accurate CSCM utilizing the spatial and temporal uniformity takes advantage of the high observation frequency of the geostationary satellite. The possible variation of the T_{b11} within a small area is investigated in detail. The most unknown cause of the variability is due to the water vapor variation within the small area. We use $T_{b11} - T_{b12}$ for a surrogate of the water vapor contents and its variability within the small area. The estimated natural variability of T_{b11} within 3×3 IFOV of GMS-5 is about $0.8°$C and is used for the threshold value for the cloud screening.

We use an empirical constant to remove erroneous clear-sky T_{b11} from the sets of the potential clear-sky T_{b11}. The constructed CSCM shows the ocean currents in great detail and compares fairly well with the NOAA weekly averaged SST distribution. The cloud edge and broken clouds are further removed from the brightness temperature difference field by using the variance obtained in the small area. The high water
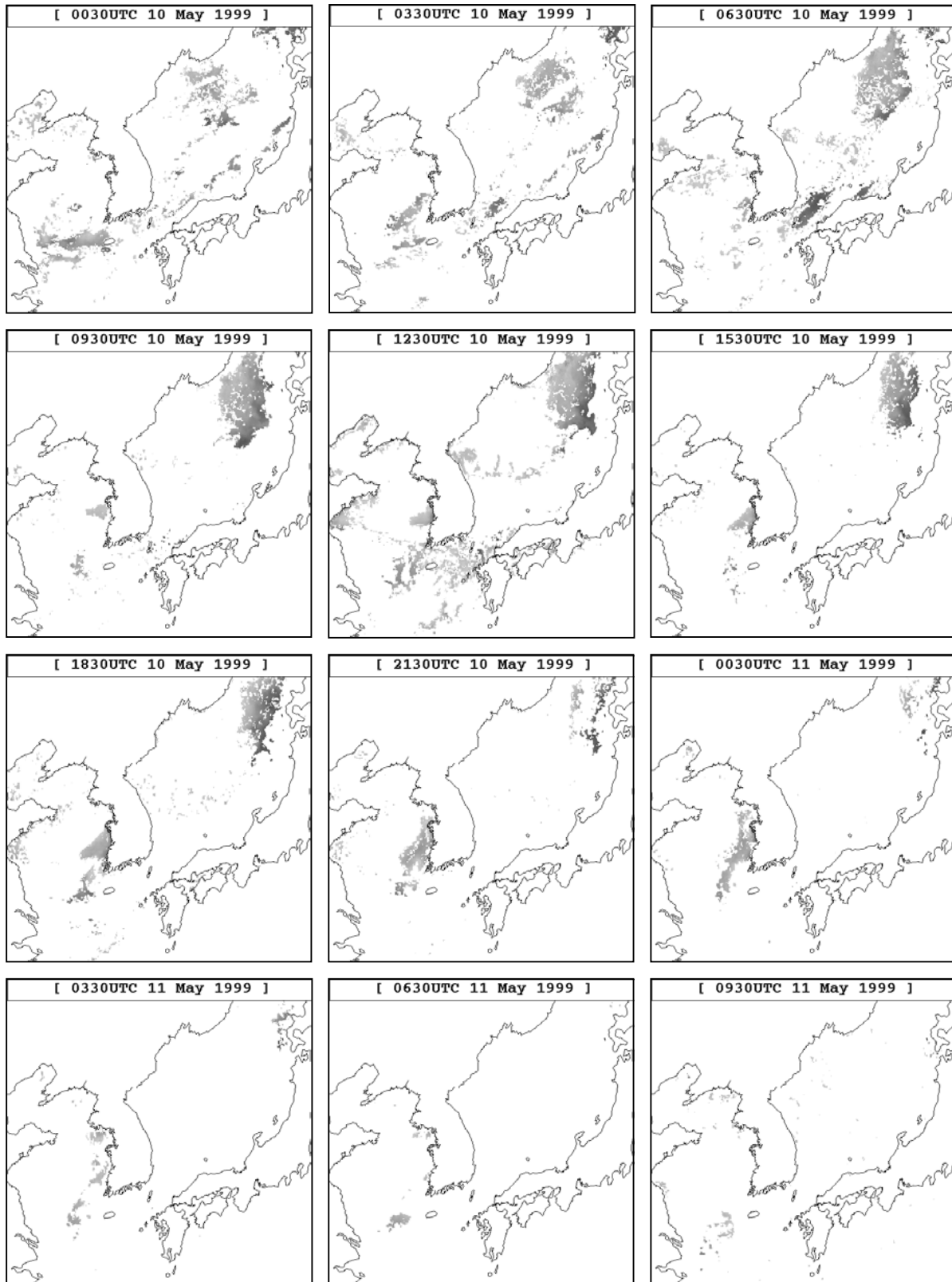
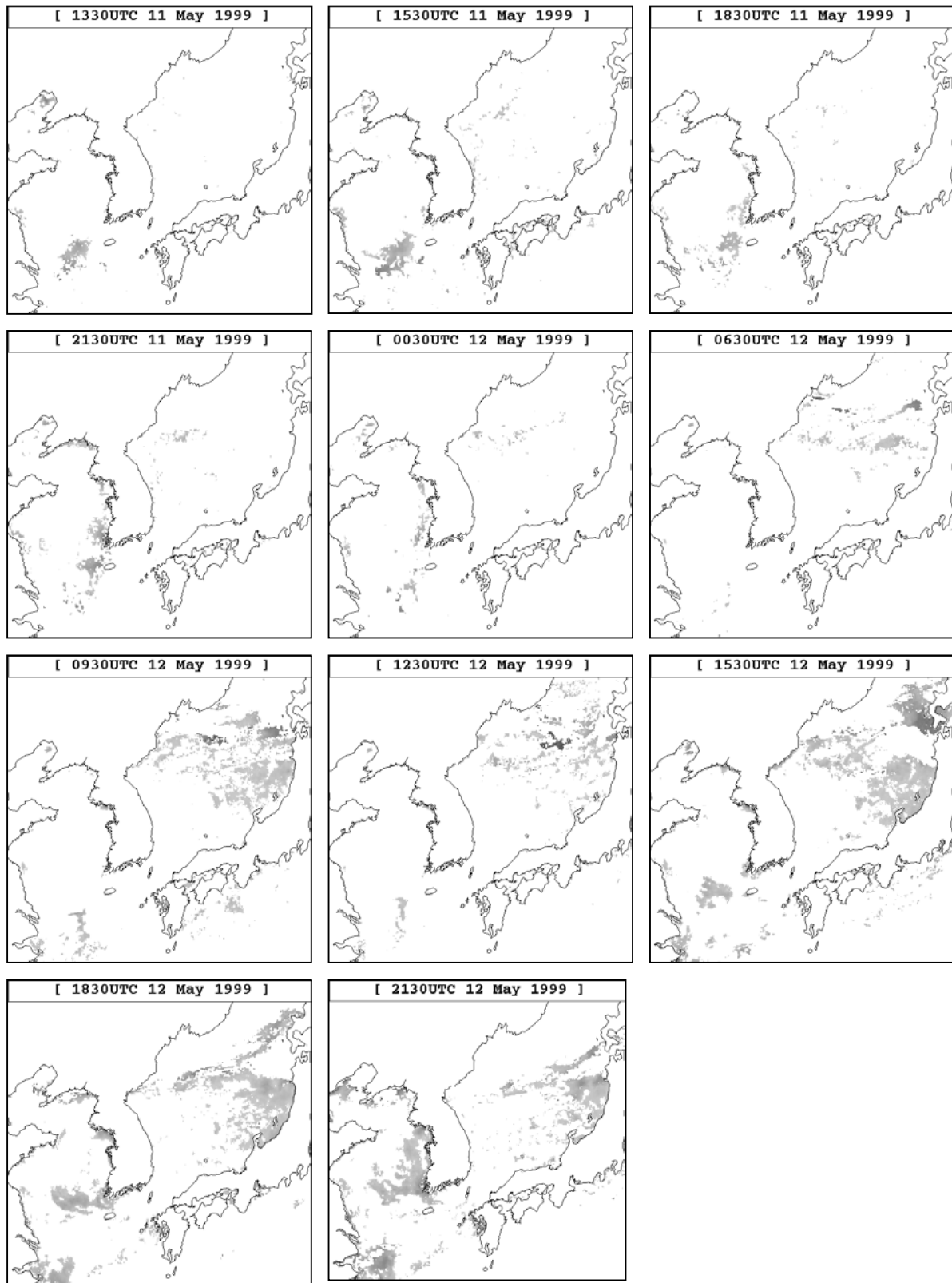**Fig. 15.** A time series of the detected fog/stratus from 10–11 May 1999.

Fig. 15. (Continued)

vapor loaded area is removed by the split window test. The comparisons between the results from the new algorithm and from either NOAA/DCD during the nighttime or the earth albedo method during the daytime show a fairly good agreement. However, we should also mention that the current method does not discriminate between fog and stratus, although a model-predicted temperature and humidity data could be used for an approximate differentiation between these two low-level clouds.

Finally, we may not be able to detect fog/stratus when a warm air mass advects over the cold ocean surface and generates fog/stratus which has a warmer top temperature than the surface, or when a radiation fog is formed below a strong conversion layer simply because of the vertical temperature profile. For a truly continuous and effective monitoring of fog, such as the advection of sea fog to inland, a method to detect fog/stratus over land, especially during the nighttime, is highly needed. As the temperature over land varies so rapidly, we may have to use not only the hourly T_{b11}, but also the surface temperature obtained from the ground observation network. Continuous comparisons of current results to the other results from other satellite sensors, such as Terra/MODIS (MODerate resolution Imaging Spectroradiometer) and direct observations either from ground or ship observation are underway. The results will also be very valuable for the future MTSAT-1R (MulTi-purpose SATellite) satellite that will be equipped with the 3.9-μm channel for a validation study. The current algorithm could also be vital as a backup if there is a failure of the shortwave IR detector on the MTSAT series or GOES-9, which is the short-term replacement of the current GMS-5. Finally, the FY-2B data could be used for the fog/stratus detection with a simple modification of the current algorithm.

REFERENCES

Anthis, A. L., and A. P. Gracknell, 1998: Fog detection and forecast of fog dissipation using both AVHRR and METEOSAT data. 9th Sat. Met/OCEAN, p2.42B, 270–273.

Anderson, G. P., and coauthors, 1995: FASCODE/ MODTRAN/LOWTRAN: Past/Present/Future, 18th Ann. Rev. Conf. Atm. Transmission Models.

Coakley, J. A., and F. P. Bretherton, 1982: Cloud cover from high resolution scanner data: Detection and allowing for partially filled fields of view. *J. Geophys. Res.*, **87**, 4917–4932.

Coakley, J. A., and D. G. Baldwin, 1984: Towards the objective analysis of clouds from satellite imagery. *J. Climate Appl. Meteor.*, **23**, 1065–1099.

Croft, P. J., R. L. Pfost, J. M. Meldin, and G. A. Johnson, 1997: Fog forecasting for the southern region: A conceptual model approach. *Weather and Forecasting*, **12**, 535–556.

Ellrod, G. P., 1995: Advances in the detection and analysis of fog at night using GOES multispectral infrared imagery. *Weather and Forecasting*, **10**, 606–619.

Ernst, J. A., 1975: Fog and stratus "invisible" in meteorological satellite infrared (IR) imagery. *Mon. Wea. Rev.*, **103**, 1024–1026.

Eyre, J. R., J. L. Brownscombe, and R. J. Allam, 1984: Detection of fog at night using Advanced Very High Resolution Radiometer. *Meteor. Mag.*, **113**, 266–271.

Inoue, T., 1985: On the temperature and effective emissivity determination of semi-transparent cirrus cloud by bi-spectral measurements in the 10 m window region. *J. Meteor. Soc. Japan*, **63**, 88–99.

Kim, M. O., 1998: The characteristics of the sea fog around the Korean Peninsula. M. S. thesis, Chonnam National University, 64pp.

Lee, T. F., F. J. Turk, and K. Richardson, 1997: Stratus and fog products using GOES-8-9 3.9-m data. *Weather and Forecasting*, **12**, 664–677.

Masuda, K., T. Takashima, and Y. Takayama, 1988: Emissivity of pure and sea waters for the model sea surface temperature in the infrared regions. *Remote Sens. Environ.*, **24**, 313–329.

METRI, 1999: Study on sea fog detection using GMS-5 satellite data (II). Meteorological Research Institute of Korea, Seoul, 73pp.

MSC, 1997: The GMS User's Guide. Meteorological Satellite Center of Japan, 190pp.

Park, K. -A., 1996: Spatial and temporal variability of sea surface temperature and sea level anomaly in the East Sea using satellite data (NOAA/AVHRR, TOPEX). Ph. D. dissertation, Seoul National University, 294pp.

Roden, G. I., 1975: On the North Pacific temperature, salinity, sound velocity and density fronts and their relation to the wind and energy flux field. *J. Phys. Oceanogr.*, **4**, 168–182.

Roozekrans, J. N., and G. J. Prangsma, 1986: Cloud clearing algorithms without AVHRR channel 3. Summary Proceeding of Second AVHRR Users Meeting, April 1986.

Saunders, R. W., and K. T. Kriebel, 1988: An improved method for detecting clear sky and cloudy radiance from AVHRR data. *Int. J. Remote Sens.*, **9**, 123–150.

Yasuda, H., and Y. Shirakawa, 1999: Improvement of the derivation method of sea surface temperature from GMS-5 data. *Meteorological Satellite Center Technical Note*, **37**, 19–33.